


Article

Different Cooling Histories of Ultrahigh-Temperature Granulites Revealed by Ti-in-Quartz: An Electron Microprobe Approach

Di Zhang ^{1,2}, Yi Chen ^{1,2,*} , Qian Mao ¹, Shujuan Jiao ¹, Bin Su ¹, Si Chen ³ and Kyaing Sein ⁴

- ¹ State Key Laboratory of Lithospheric Evolution, Institute of Geology and Geophysics, Chinese Academy of Sciences, Beijing 100029, China; zhangdi@mail.iggcas.ac.cn (D.Z.); maoqian@mail.iggcas.ac.cn (Q.M.); jiaoshujuan@mail.iggcas.ac.cn (S.J.); subin@mail.iggcas.ac.cn (B.S.)
- ² College of Earth and Planetary Sciences, University of Chinese Academy of Sciences, Beijing 100049, China
- ³ Guangzhou Marine Geological Survey, Guangzhou 511458, China; chen_si@vip.163.com
- ⁴ Myanmar Geosciences Society, Hlaing University Campus, Yangon 11041, Myanmar; kyaingsein@gmail.com
- * Correspondence: chenyi@mail.iggcas.ac.cn; Tel.: +86-010-8299-8534

Abstract: The cooling history of granulite is crucial to understanding tectonic scenarios of the continental crust. Ti-in-quartz, a useful indicator of temperature, can decipher the thermal evolution of crustal rocks. Here we apply the Ti-in-quartz (TitaniQ) thermometer to ancient ultrahigh-temperature (UHT) granulites from the Khondalite Belt (KB) in the North China Craton (NCC) and young UHT granulites from the Mogok Metamorphic Belt (MMB), Myanmar. Ti content in quartz was analyzed using a highly precise method constructed in a CAMECA SXFive electron probe microanalyzer (EPMA). The granulites from the two localities show different quartz Ti contents with a constant defocused beam of 10 μm . Matrix quartz and quartz inclusions from the NCC granulites have 57–241 ppm and 65–229 ppm, respectively, corresponding to the TitaniQ temperatures of 653–810 $^{\circ}\text{C}$ and 666–807 $^{\circ}\text{C}$. The calculated temperatures are significantly lower than the peak temperatures (850–1096 $^{\circ}\text{C}$) obtained by other methods, due to the formation of abundant rutile exsolution rods in quartz during cooling. Thus, the low calculated temperatures for the NCC granulites reflect a cooling state near or after the exsolution of rutile from quartz, most likely caused by a slow cooling process. However, the matrix quartz from the MMB granulites is exsolution-free and records higher Ti contents of 207–260 ppm and higher metamorphic temperatures of 894–926 $^{\circ}\text{C}$, close to the peak UHT conditions. This feature indicates that the MMB granulites underwent rapid cooling to overcome Ti loss from quartz. Therefore, determining the amount of Ti loss from quartz by diffusion can provide new insight into the cooling behavior of UHT granulites. When a large defocused beam of 50 μm was used to cover the rutile rods, the matrix quartz in the KB granulites could also yield the TitaniQ temperatures above 900 $^{\circ}\text{C}$. Thus, our new data suggest that the TitaniQ thermometer could be useful for revealing UHT conditions.

Keywords: TitaniQ thermometer; UHT granulites; cooling behavior; electron probe microanalysis; diffusion



Citation: Zhang, D.; Chen, Y.; Mao, Q.; Jiao, S.; Su, B.; Chen, S.; Sein, K. Different Cooling Histories of Ultrahigh-Temperature Granulites Revealed by Ti-in-Quartz: An Electron Microprobe Approach. *Crystals* **2023**, *13*, 1116. <https://doi.org/10.3390/cryst13071116>

Academic Editor: Vladislav V. Gurzhiy

Received: 2 July 2023

Revised: 12 July 2023

Accepted: 15 July 2023

Published: 17 July 2023



Copyright: © 2023 by the authors. Licensee MDPI, Basel, Switzerland. This article is an open access article distributed under the terms and conditions of the Creative Commons Attribution (CC BY) license (<https://creativecommons.org/licenses/by/4.0/>).

1. Introduction

Ultrahigh-temperature (UHT) metamorphism, a thermally extreme crustal metamorphism with temperatures exceeding 900 $^{\circ}\text{C}$ within the sillimanite stability field, is crucial for understanding the thermal evolution of the continental crust [1]. To date, over 70 UHT metamorphic localities have been identified worldwide, spanning from Archean to Cenozoic [2,3]. These UHT granulites exhibit different duration time and cooling rates [3,4]. Therefore, obtaining accurate peak and post-peak temperatures and time scales for UHT granulites could provide key constraints on the thermotectonic and/or geodynamic models of the crust. However, temperature constraint is one of the challenges for identifying UHT

metamorphism. Conventional thermometers commonly yield high temperatures (HT) for UHT granulites due to the diffusion and resetting of major elements (such as Fe-Mg) during cooling [5,6]. Moreover, phase equilibria modeling allows to evaluate the metamorphic conditions and processes in UHT granulites and the diffusion of major elements in minerals [3]. The progress of trace-element thermometers, including Zr-in-rutile [7–10], Ti-in-zircon [8,9,11], and TitaniQ thermometers [12–15], would have improved our ability to constrain UHT conditions and understand thermally extreme deep crustal processes.

As one of the most abundant rock-forming minerals in the crust, quartz has considerable Ti^{4+} that can substitute for Si^{4+} in the crystal lattice or can be incorporated in interstitial positions. The TitaniQ thermometer has been widely used to calculate the formation temperatures of metamorphic and magmatic rocks [15–18]. However, the ability to recover UHT metamorphic conditions by the TitaniQ thermometer is still debated [3,13] due to the faster diffusion rate of Ti-in-quartz than those of Zr-in-rutile and Ti-in-zircon [19]. The results of the TitaniQ thermometer in granulites are significantly influenced by late-stage resetting [16,20,21]. Understanding the meaning of the TitaniQ temperatures in UHT granulites requires both high spatial resolution and precision of Ti measurements in quartz.

Modern microbeam tools with a high spatial resolution have been applied to quartz, including secondary ion mass spectrometry (SIMS), laser ablation inductively coupled plasma mass spectrometry (LA-ICP-MS), and electron microprobe [22–29]. SIMS has the highest precision and capability of hydrogen analysis, but this approach requires high-quality matrix-matched reference materials [28]. For LA-ICP-MS, although multi-analyzing can be performed with a low detection limit, the results are easily affected by various forms of interferences and fractionation and by memory effects [30,31]. Additionally, quartz has a low degree of laser absorbance efficiency and thus may sputter under laser ablation, which notably impacts the stability of signals [32]. In particular, the spatial resolution of SIMS and LA-ICP-MS (>20 μm) cannot resolve the tiny and complex areas commonly observed in metamorphic quartz. Compared to the above two approaches, EPMA achieves the highest level of spatial resolution while remaining nondestructive analysis. In addition, granulite quartz has considerable Ti concentrations, usually exceeding the detection limit of EPMA [21,33]. Therefore, EPMA can provide high-precision analysis of Ti-in-quartz with a high spatial resolution below 10 μm .

In this study, we performed a precise trace-element analysis of quartz using a CAMECA SXFive electron microprobe at the Institute of Geology and Geophysics, Chinese Academy of Sciences (IGGCAS), China, which produces analyses of Al and Ti with a precision better than 6 ppm (2SD). The analytical method was tested by analyzing the well-certified quartz standard developed by Audétat et al. [28]. We applied this method to a set of ancient (Paleoproterozoic) UHT granulites from the NCC (China) and young (Cenozoic) UHT granulites from the MMB (Myanmar). Our results show that the TitaniQ thermometer, coupled with microtextures of quartz, can not only recognize UHT metamorphism, but also provide new insights into the cooling behavior of UHT granulites at different geological periods.

2. Geological Setting and Sample Descriptions

2.1. Granulites from the Khondalite Belt, North China Craton

The Paleoproterozoic Khondalite Belt (KB) is located in the Western Block of the NCC (Figure 1) and was formed by the collision of the Ordos Block in the south with the Yinshan Block in the north at ca.1.95 Ga [34–37]. It extends around 750 km in the E–W direction [34] and is divided into three terranes from west to east: Helanshan–Qianlishan, Daqingshan–Ulashan, and Jining. The Khondalite Belt mainly consists of granulite-facies quartzo-feldspathic gneiss, garnet–sillimanite gneiss, feldspathic quartzite, marble, and calc-silicate rocks [38]. Ultrahigh-temperature assemblages have been identified from several localities in the eastern KB [38–43]. Diagnostic UHT mineral assemblages of sapphirine + quartz and orthopyroxene + sillimanite \pm quartz are well preserved in Dongpo and Tianpishan [38]. Other UHT regions without diagnostic UHT mineral assemblages, such as

Xuwujia and Tuguishan, were also distinguished by two-feldspar geothermometry, Fe-Ti oxides geothermometry, and Zr-in-rutile thermometry [38,39,43].

In this study, we collected UHT granulites from Tuguishan, Tianpishan, and Xuwujia in the KB. These samples are garnet–sillimanite granulites (Figure 2a). Some samples (08TPS09 and 08TPS11) contain sapphirine–quartz assemblage, thus confirming their formation under UHT conditions (Figure 2b). Other samples are also identified as UHT granulites via thermobarometric approaches [38,39]. Quartz may occur in the matrix or as inclusions in garnet with various sizes of 100–1000 μm . Rutile rods commonly occur in both types of quartz (Figure 2c,d), with lengths ranging from 5 to 100 μm .

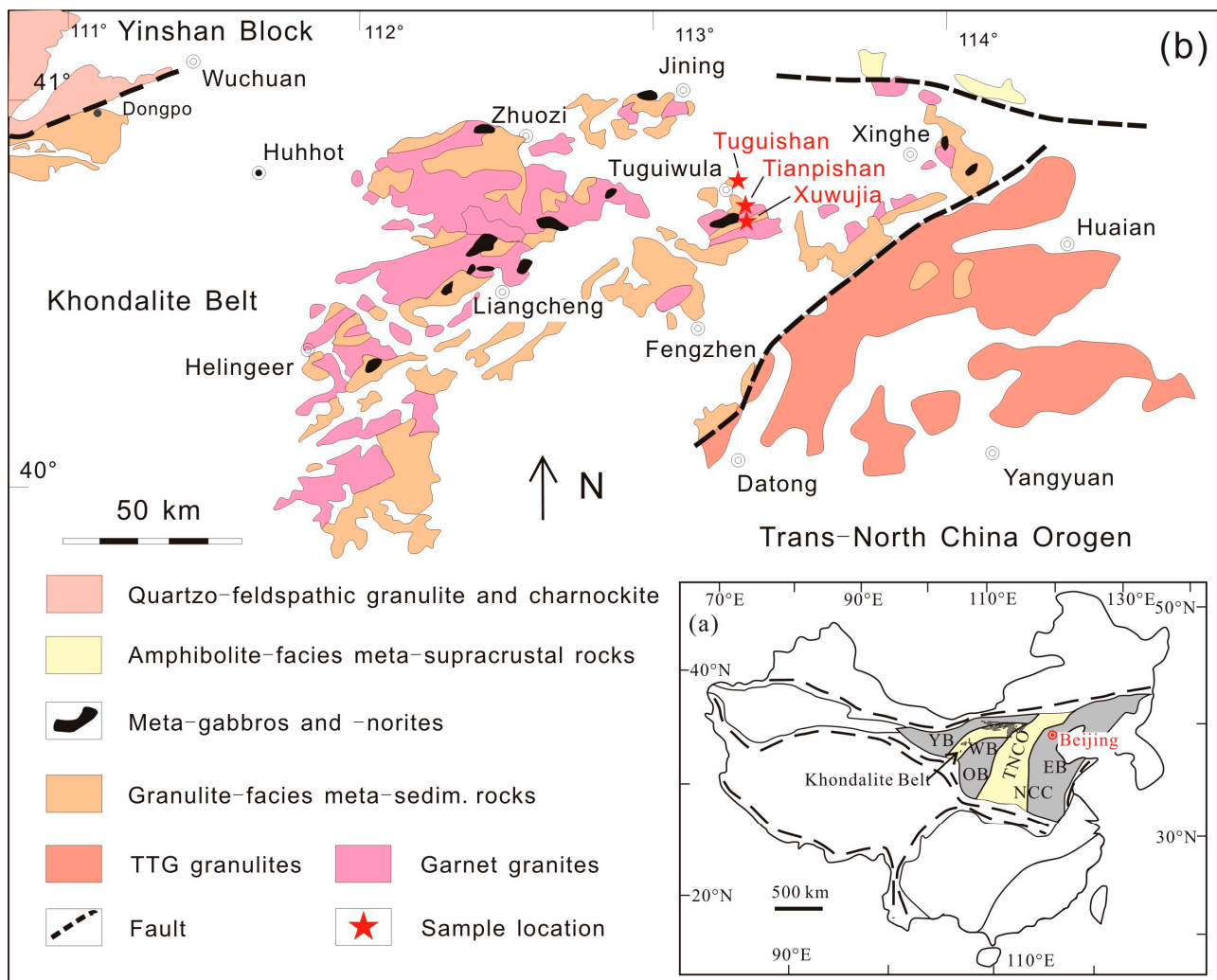


Figure 1. (a) Simplified three-fold tectonic division of the North China Craton (modified after Zhao et al. [34]). Abbreviations: EB Eastern Block, TNCO Trans-North China orogen, WB Western Block, YB Yinshan Block, KB Khondalite Belt, IMSZ Inner Mongolia Suture Zone, OB Ordos Block. (b) Distribution of the high-grade metamorphic rocks in the eastern segment of the Khondalite Belt, North China Craton, and the studied areas (modified after Guo et al. [44]).

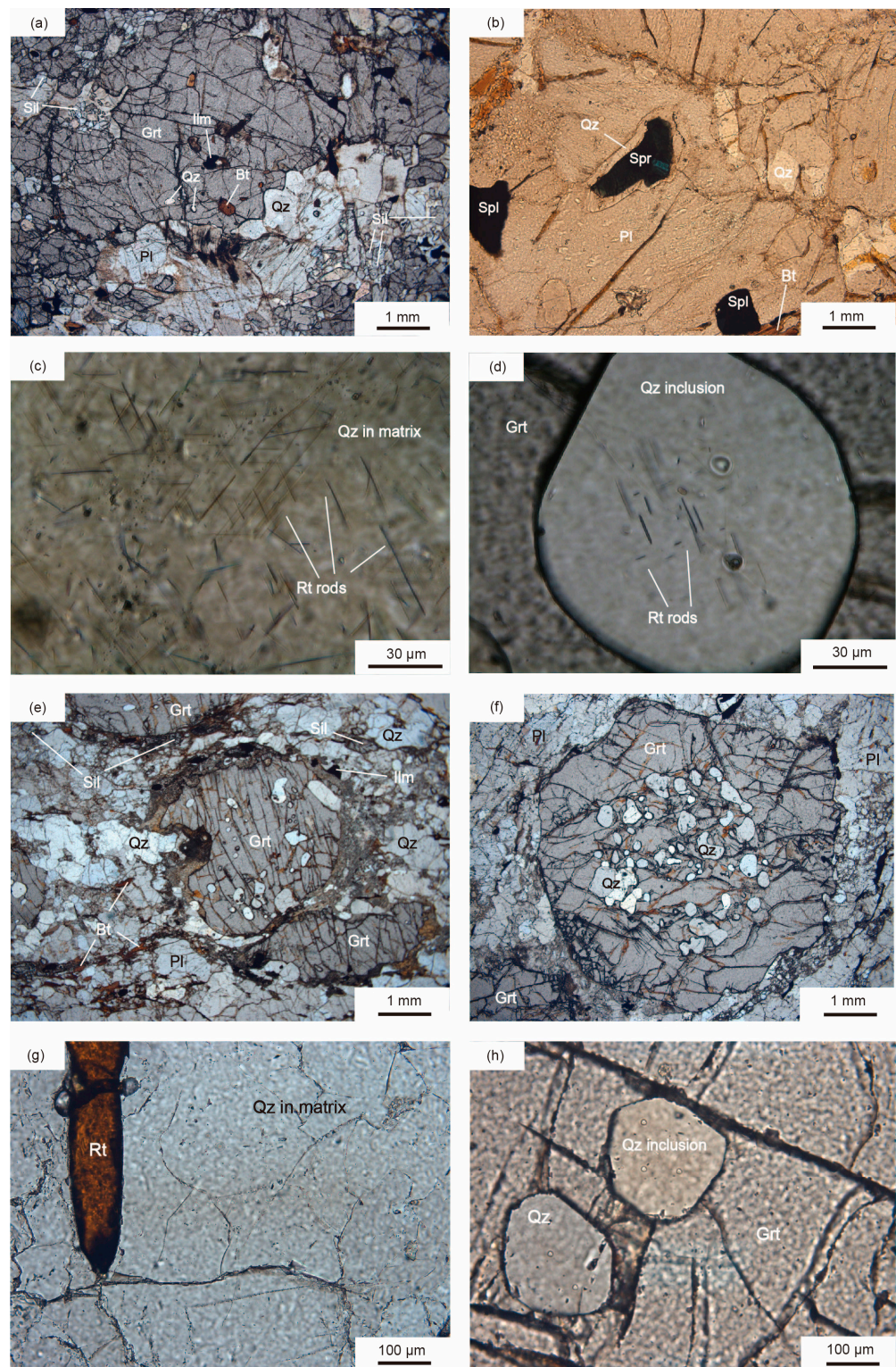


Figure 2. Photomicrographs showing microtextures of quartz grains from the investigated samples. (a) Garnet, sillimanite, quartz, plagioclase, biotite, and ilmenite in garnet-sillimanite granulite from Tuguishan area in the KB (08TG06B). (b) Sapphirine, spinel, plagioclase, biotite, and quartz in garnet-sillimanite-sapphirine granulite from Tianpishan in the KB (08TPS-11). (c) Rutile rods in matrix quartz (08TG06A). (d) Rutile rods in quartz inclusions in garnet (08XWJ01). (e) Garnet, plagioclase, quartz, sillimanite, biotite, and ilmenite in garnet granulite from the MMB (19MDL115-3). (f) Garnet, plagioclase, and quartz in garnet granulite from the MMB (19MDL126-1). (g) Quartz grains occur in the matrix coexisting with rutile (19MDL115-2). (h) Quartz inclusions in garnet (19MDL126-2).

2.2. Granulites from the Mogok Metamorphic Belt, Myanmar

The MMB is located between the central Burma basin and Shan Plateau and extends for approximately 1500 km from the Andaman Sea to the eastern Himalaya syntaxis (Figure 3a) [45–49]. Metamorphic rocks in the MMB, including schists, gneisses, migmatites, gem-bearing (such as ruby, sapphire, and spinel) marbles, calc-silicate rocks, and quartzites, formed under amphibolite-to granulite-facies conditions [45–47]. Searle et al. [47] proposed that two Tertiary metamorphic events occurred in the MMB, including a Paleocene metamorphism and an Eocene to Oligocene metamorphism. The main lithologies exposed near Mogok are gem-bearing marbles, garnet–sillimanite granulites, and calc-silicate rocks, representing a regional high-temperature metamorphic unit (Figure 3b). Syenite, leucogranite, biotite microgranite, pegmatite, and ultramafic rocks also occur in this region (Figure 3b). The widespread garnet–sillimanite granulites from Mandalay to Mogok record peak P–T conditions of 6–10 kbar and 780–950 °C [50–53]. Based on a combined study of petrology and geochronology, Chen et al. [54] reported the discovery of ~25 Ma UHT granulites from Htin-Shu-Taung and Panlin in the Bernardmyo area, north Mogok, with peak P–T conditions of ~12 kbar and >900 °C. The $^{40}\text{Ar}/^{39}\text{Ar}$ ages of mica from the MMB granites, marbles, gneisses, and mica schists are mostly 22.7–15.8 Ma [55–57], pointing to an Oligocene to Miocene cooling age.

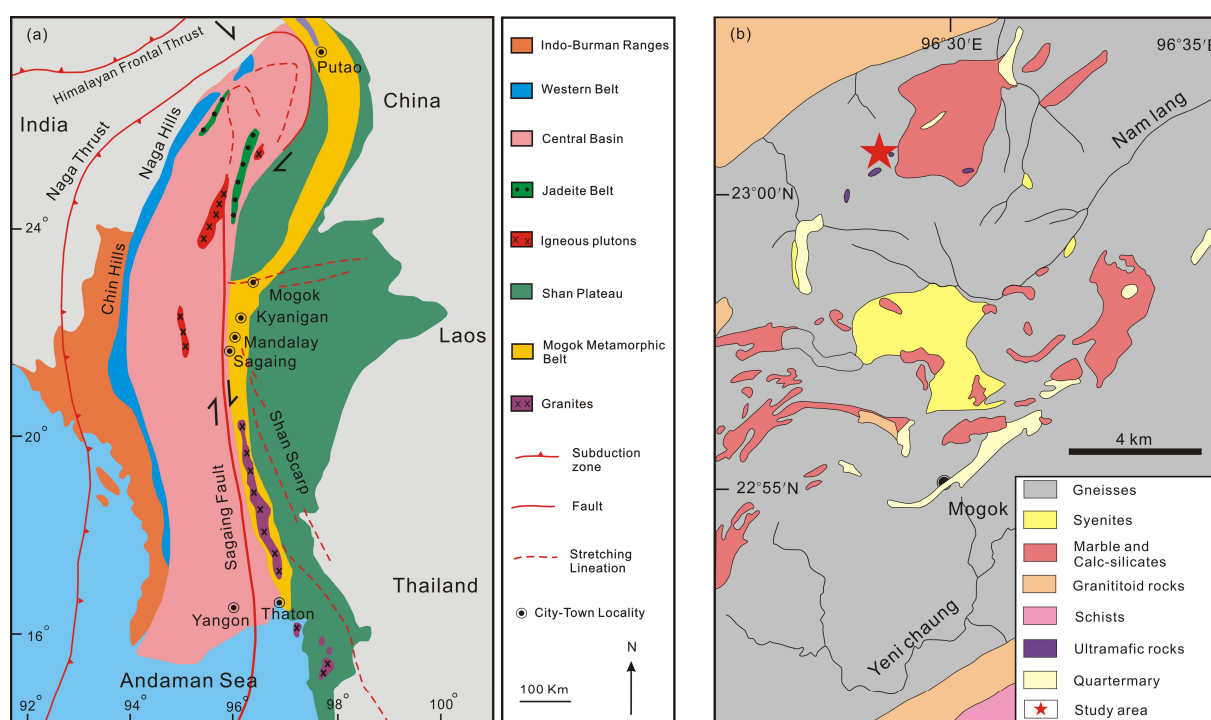


Figure 3. (a) A schematic geological map (modified after Themelis [58]) showing the principal structural features and terrane boundaries of Myanmar and the distribution of the MMB. (b) Geological map of the Mogok area (modified after Mitchell et al. [46]).

The studied UHT granulites were collected from the same outcrop as site 1 in Chen et al. [54], Htin-Shu-Taung (96°28′40″ E, 23°0′50″ N) in the Bernardmyo area, north Mogok (Figure 3b). They preserve typical granulite-facies assemblage of garnet–sillimanite–K-feldspar and mainly consist of garnet (30–35%), quartz (25–30%), sillimanite (10–15%), antiperthite (~10%), k-feldspar (~10%), rutile (<5%), biotite (<5%) and ilmenite (<1%) (Figure 2e,f, Table 1). Zr-in-rutile thermometer and pseudosection modeling indicate that these granulites underwent UHT metamorphism during the Cenozoic [54]. Quartz occurs in the matrix or as inclusions in garnet. No rutile rods have been observed in thin sections (Figure 2g,h).

Table 1. Mineral assemblages in the investigated samples.

Locality	Lithology	Sample	Peak Mineral Assemblage ¹
<i>Khondalite Belt, North China Craton</i>			
Tuguishan	Grt–Sil granulite	08TG06A, 08TG06B	Grt + Sil + Spl + Kfs + Pl + Bt + Qz + Rt + Zrn + Ilm
Tianpishan	Garnet–sillimanite–sapphirine granulite	08TPS09, 08TPS11	Grt + Sil + Spr + Spl + Kfs + Pl + Qz + Opx + Rt + Zrn + Ilm
Xuwujia	Grt–Sil–Bt–Pl granulite	08XWJ01	Grt + Sil + Kfs + Pl + Qz + Rt ± Bt + Zrn + Ilm
<i>Mogok Metamorphic Belt, Myanmar</i>			
Htin-ShuTaung	Grt granulite	19MDL115-2, 19MDL115-3, 19MDL119-2, 19MDL126-1, 19MDL126-2	Grt + Sil + Pl + Kfs ± Bt + Rt + Qz + Zrn + Ilm

¹ Abbreviations of mineral names are after Whitney and Evans [59].

3. Analytical Methods

Trace elements (Ti and Al) of quartz were analyzed using the CAMECA SXFive electron microprobe at IGGCAS. To determine the optimal accelerating voltage, beam current, and peak counting time for analyzing Al and Ti-in-quartz, we conducted a set of experiments following the steps developed by Batanova et al. [60]. A quartz reference material was tested at 15, 20, and 25 kV with beam currents (measured with a Faraday cup) of 20, 50, 100, 200, 300, 400, 500, and 600 nA, respectively. The other operating conditions were employed as follows: a peak counting time of 240 s, a beam size of 10 μm, and linear background mode. Rutile and albite were used as primary standards for calibration. Standardization was performed with 20 nA beam current and 20 s peak counting time. The detection limit was determined with CAMECA software using background statistics and the 3-sigma criterion as recommended by Ancey et al. [61]. Other analytical conditions are listed in Table S1A. Figures S1 and S2 show that the detection limit (3σ) and standard deviation (3σ) for a single point are inversely proportional to beam current and peak counting time. However, the detection limit and standard deviation only show slight changes under beam current over 300 nA and peak counting time beyond 240 s. Considering analytical efficiency and precision, we select a beam current of 300 nA and a peak counting time of 240 s as the optimal conditions. In addition, although higher accelerating voltage can lower the detection limit, it would also reduce spatial resolution and increase absorption corrections. To balance these effects, a 15 kV accelerating voltage normally used in major element analysis is an adequate choice when analyzing Al and Ti-in-quartz. Moreover, using an appropriate diffraction crystal and aggregate intensity counting method is conducive to reducing detection limits and improving precision levels [26]. As shown in Figure S2, the detection limit obtained by the standard crystal (PET, red line in Figure S2) is the highest, followed by that obtained by the large-area Bragg crystals (LPET, green line in Figure S2), while that obtained via the aggregate intensity counting method is the lowest (blue line in Figure S2). The standard deviation for a single point also shows the same variation (Figure S2b,d). Therefore, two spectrometers equipped with TAP crystals were selected to analyze Al, while two with LPET crystals were selected for analyzing Ti-in-quartz.

We run the quartz reference standard [28] as an unknown sample for 25 points to evaluate the accuracy and precision of the above-constructed method. The analytical precision (reproducibility) of quartz analyses, established by repeated measurement of quartz standard, is 4 to 6 ppm for Al and Ti (2sd, $n = 25$, Table S1B). Each analysis has three standard deviations of 7 to 8 ppm. The average values of the continuous 25 analyses for Al and Ti are 152 ± 6 ppm and 56 ± 4 ppm (2sd) (Table S1B, Figure 4a,b), respectively, which are consistent with the reference values (Al: 154 ± 15 ppm, Ti: 57 ± 4 ppm) within error [28]. All the analytical results vary within $\pm 6\%$. The total analytical time of this method is only 9 min. In addition, to evaluate the reproducibility of the data, 13 points were analyzed

over an interval of two hours. As shown in Figure 4c, the results are consistent with the recommended values. The analysis of Al shows higher stability than that of Ti, with concentrations clustering at 152 ppm and fluctuations falling within $\pm 5\%$. All these results indicate that our facility and analytical method are stable and precise in trace-element analysis of quartz.

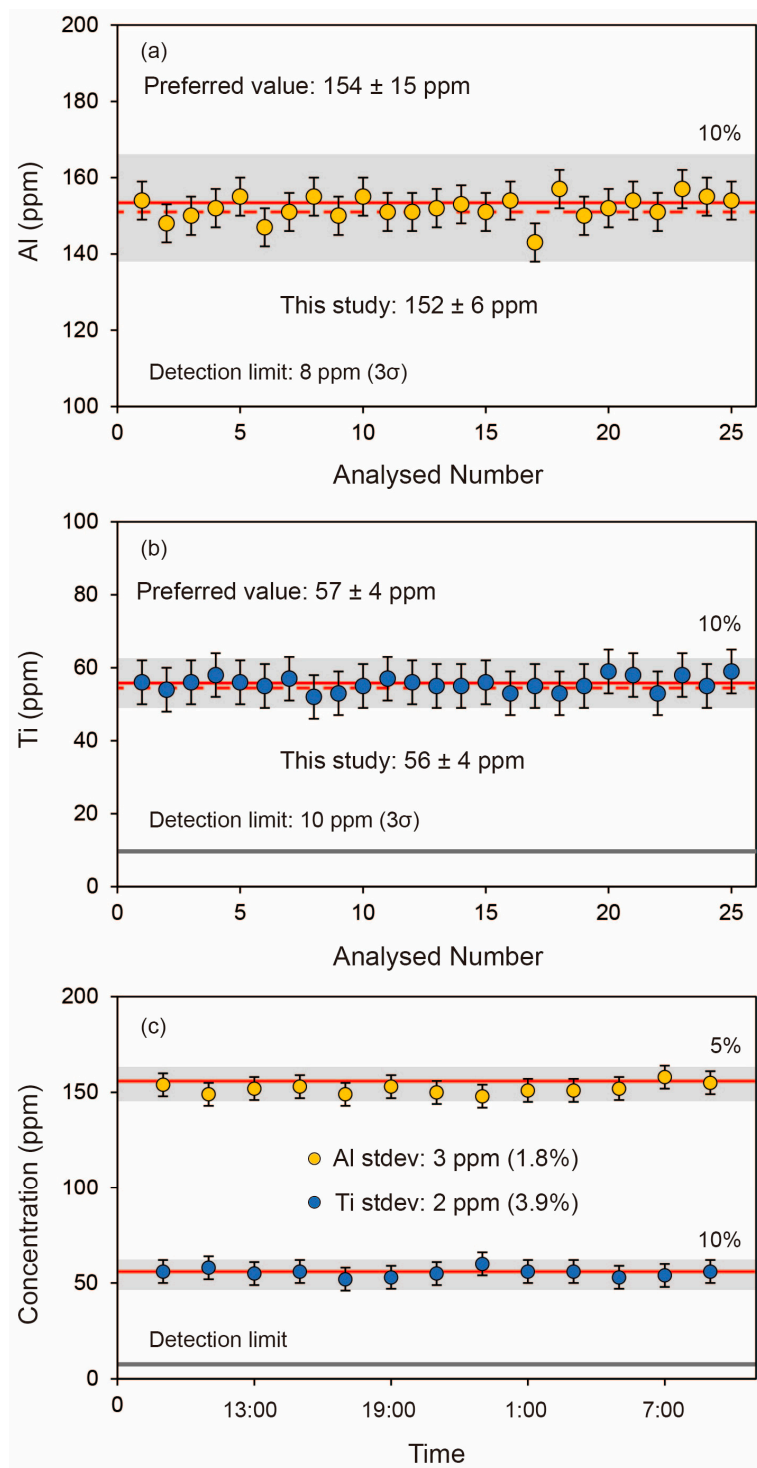


Figure 4. Twenty-five data results on the reference standard for Al (a) and Ti (b). Stability of trace-element data from the quartz reference standard (c). The shaded portion represents the 10% margin of error. The solid line represents the recommended value, and the dotted line represents the average value. Error bars = two standard deviations.

To reduce beam damage, quartz grains in granulites from both localities were analyzed with a defocused beam of 10 μm . As exsolved rutile rods commonly occur in quartz in the KB granulites, we additionally adopt a larger defocused beam of 50 μm to overlap the rods. This approach can reintegrate the pre-exsolution Ti concentration of quartz.

Secondary fluorescence effect is common in trace Ti analysis in quartz. Here we performed a profile of quartz adjacent to large rutile grains with 10 μm beam size. As shown in Figure S3, the apparent Ti concentration in quartz reaches up to 1490 ppm at 10 μm from rutile and gradually decreases away from rutile (Table S1C). The measured Ti concentration becomes constant at ~ 170 μm from large rutile grain. Therefore, we analyzed quartz grains at least 200 μm away from large rutile grains to avoid secondary fluorescence effects. To precisely obtain the Ti concentration of quartz after rutile exsolution in the KB samples when using 10 μm beam size, we analyzed quartz away from rutile rods as far as possible. The analytical results should not be greatly influenced by secondary fluorescence effects due to the small volume of rutile rods, as suggested by Storm and Spear [21].

4. Results

The Ti concentrations of quartz from the studied granulites are listed in Tables S2–S5. All outliers are excluded from discussion. The quartz from the KB (Tuguishan, Tianpishan, and Xuwujia) granulites shows a wide Ti variation under the beam size of 10 μm (Figure 5a). The Ti concentrations of the matrix quartz from the Tuguishan, Tianpishan, and Xuwujia samples are 57–233 ppm ($n = 43$), 83–241 ppm ($n = 55$), and 70–124 ppm ($n = 29$), respectively, whereas those of the quartz inclusions in garnet are 65–208 ppm ($n = 49$), 75–229 ppm ($n = 60$), and 81–140 ppm ($n = 28$), respectively. The large variations can be observed even in the same thin section (Tables S2–S4). The textural setting of quartz (inclusion vs. matrix) has not significantly affected Ti concentrations. Moreover, the Ti concentrations have no relation with grain size and exhibit similar values in a single grain.

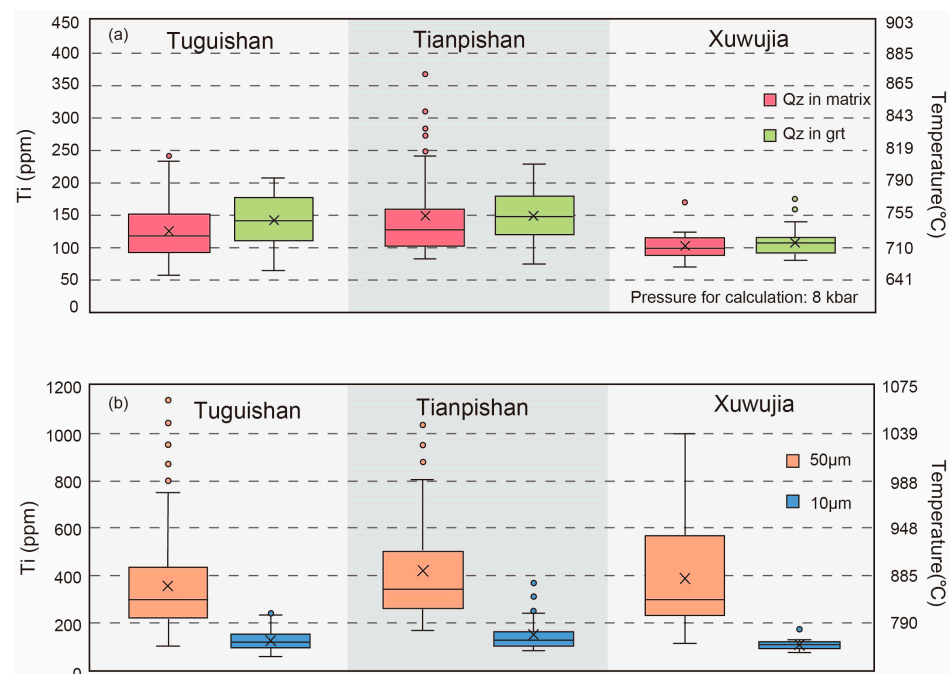


Figure 5. Summary of Ti concentrations and calculated temperatures for the studied quartz from the Khondalite Belt, North China Craton. (a) Ti concentrations of various textural quartz and calculated temperatures (beam size: 10 μm). (b) Ti concentrations of matrix quartz under the beam size of 50 μm and 10 μm and the calculated temperatures. From bottom to top, the boxes represent the second and third quartiles (25% and 75% of the population). The transverse line inside the box represents the median, while the cross represents the average. The whiskers represent the highest and lowest values. Outliers, if they occur, are represented by small circles.

To recover the pre-exsolution Ti concentrations of the matrix quartz, we use a larger beam size of 50 μm additionally. The newly analytical results of the Tuguishan, Tianpishan, and Xuwujia samples are 99–753 ppm ($n = 102$), 169–806 ppm ($n = 48$), and 112–1001 ppm ($n = 41$), which overall are higher than those obtained using the 10 μm beam size (Figure 5b). Furthermore, the average Ti concentrations acquired using the 50 μm beam size in each granulite (355–419 ppm) are also higher than those obtained using the 10 μm beam size (103–149 ppm).

In contrast, the quartz from the Mogok granulites shows systematically high Ti concentrations (107–267 ppm, $n = 281$). The textural setting of quartz (inclusion vs. matrix) significantly affects the Ti concentrations (Figure 6a). The quartz inclusions in garnet have variable Ti contents of 107–267 ppm (Table S5, $n = 138$); however, the matrix quartz has more constrained and relatively higher Ti contents of 207–260 ppm (Figure 6a, $n = 143$). In addition, quartz grains, both in the matrix and inclusions, do not show Ti zoning.

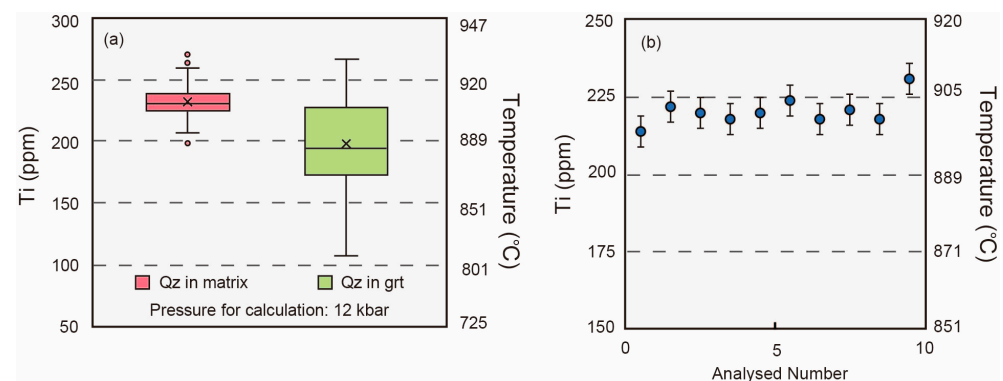


Figure 6. Summary of Ti concentrations and calculated temperatures for the studied quartz from the Mogok Metamorphic Belt, Myanmar. (a) Ti concentrations of various textural quartz and the calculated temperatures (beam size: 10 μm). (b) Ti concentrations and calculated temperatures of quartz inclusion in garnet from the MMB profiled by EPMA. Error bars = 2 standard deviations. From bottom to top, the boxes represent the second and third quartiles (25% and 75% of the population). The transverse line inside the box represents the median, while the cross represents the average. The whiskers represent the highest and lowest values. Outliers, if they occur, are represented by small circles.

Profile analysis is taken in quartz inclusion with a length of 200 μm (Figure 6b, Table S6). The profile exhibits little fluctuations in the Ti concentrations (214–231 ppm, $n = 10$) from core to rim. The Ti concentrations of the profile are at the same level as those of matrix quartz.

5. Temperature Estimation Based on TitaniQ Thermobarometer

Many TitaniQ thermometer models are proposed [8,13–15,62,63]. The TitaniQ thermometer was first constructed by Watson et al. [8] in detail, based on experimental results at 600–1000 $^{\circ}\text{C}$ and 10 kbar. However, this early version has no pressure corrections. Within other models, the experiments were conducted at 600–1000 $^{\circ}\text{C}$ and 5–20 kbar in the Thomas et al. [13] model, which is the most suitable for the metamorphic conditions of our studied granulites. Therefore, we use the calibration of Thomas et al. [13] in this study. Analytical uncertainty may result in an error of ± 8 $^{\circ}\text{C}$ on the TitaniQ temperatures.

Since rutile occurred in all investigated samples, the TitaniQ thermometer could be applied to calculate the temperatures with the TiO_2 activity equal to 1 [13]. Pressure plays a key role in temperature determination by the TitaniQ thermometer, with an effect of ~ 23 $^{\circ}\text{C}$ rise per 1 kbar increment. The studied KB granulites are the same as those from Jiao et al. [38], where 8 kbar was used to calculate temperatures by the Zr-in-rutile thermometer for these KB granulites. The same pressure was used for our TitaniQ thermometer calculations. Granulites from the MMB in this study were collected from the same

outcrop as site 1 in Chen et al. [54]. The pressure of 12 kbar estimated by P–T pseudosections [54] was used for calculating the TitaniQ temperatures. All temperatures are listed in Tables S2–S6 following each Ti concentration.

Figure 5a shows that quartz from the KB (Tuguishan, Tianpishan, and Xuwujia) exhibits a wide variation among calculated temperatures when using the 10 μm beam size. Calculated temperatures of matrix quartz from Tuguishan, Tianpishan, and Xuwujia are 653–810 $^{\circ}\text{C}$ ($n = 43$), 690–814 $^{\circ}\text{C}$ ($n = 55$), and 673–733 $^{\circ}\text{C}$ ($n = 29$), respectively, whereas those of the quartz inclusions in garnet are 666–795 $^{\circ}\text{C}$ ($n = 49$), 680–807 $^{\circ}\text{C}$ ($n = 60$), and 688–747 $^{\circ}\text{C}$ ($n = 28$), respectively. The peak values of temperatures were around 710–750 $^{\circ}\text{C}$. While using a larger defocused beam size of 50 μm , higher temperatures were obtained for matrix quartz (Figure 5b), e.g., 709–987 $^{\circ}\text{C}$ for Tuguishan, 769–999 $^{\circ}\text{C}$ for Tianpishan, and 722–1039 $^{\circ}\text{C}$ for Xuwujia. It is worth noting that the lowest temperatures obtained by the 50 μm beam size fall within the peak temperature range (710–750 $^{\circ}\text{C}$) obtained using 10 μm beam size. In addition, more than 30% of the analyzed quartz samples record temperatures over 900 $^{\circ}\text{C}$. The highest temperature is around 1040 $^{\circ}\text{C}$ for the Xuwujia granulite.

In comparison, the MMB quartz shows various characteristics with higher temperatures over 900 $^{\circ}\text{C}$ (Figure 6a). Temperature differences exist between quartz inclusions and quartz in the matrix. Analyses of quartz inclusions facilitate obtaining lower and more variable temperatures of 809–930 $^{\circ}\text{C}$ (Table S5). However, quartz in the matrix gives higher and more concentrated TitaniQ temperatures of 894–926 $^{\circ}\text{C}$. The average temperature of matrix quartz is 909 ± 7 $^{\circ}\text{C}$. Moreover, over 75% of the analyzed matrix quartz grains may record temperatures over 900 $^{\circ}\text{C}$.

Profile analysis of quartz inclusion shows consistent TitaniQ temperatures, commonly exceeding 900 $^{\circ}\text{C}$ (Figure 6b). Moreover, the average temperature for the profile is 903 ± 3 $^{\circ}\text{C}$, which is consistent with matrix quartz.

6. Discussion

6.1. Validation of TitaniQ Thermometer for Recording UHT Metamorphic Conditions

Since the TitaniQ thermometer was first proposed in detail 17 years ago [12], it has been widely used to calculate the formation temperatures of metamorphic and magmatic rocks [15–18]. Several previous studies also used this thermometer to identify UHT granulites [16,17,20,64–67], thus proving the feasibility of the TitaniQ thermometer in recognizing UHT metamorphism. Extremely high TitaniQ temperatures (many >1100 $^{\circ}\text{C}$) were acquired by Sato and Santosh [20]. Altenberger et al. [16] obtained highly variable temperatures and figured out that the highest temperature (8 kbar: 880 $^{\circ}\text{C}$) could be the minimum metamorphic temperature. Ewing et al. [17], Horton et al. [64], Sanborn-Barrie et al. [65], and Ramírez-Salazar et al. [66] suggested that temperatures acquired using TitaniQ thermometer could correlate well with those obtained by Zr-in-rutile thermometer.

Combining the quartz cathode luminescence characteristics and the Ti concentrations obtained by 50 μm , Zheng et al. [67] figured out that matrix quartz with extensive rutile exsolution most probably grew during the near-peak to the early cooling stage and can better constrain the near-peak conditions. Their highest TitaniQ temperatures (ca. 960–970 $^{\circ}\text{C}$) are broadly consistent with the reported temperatures calculated by other methods in the studied region from the KB [35,41,68,69]. Similarly, over 30% of the matrix quartz in this study record temperatures above 900 $^{\circ}\text{C}$ when using a larger defocused beam of 50 μm (Figure 7a–c). The highest temperature is around 1040 $^{\circ}\text{C}$ for the Xuwujia sample from the KB (Figure 7c), which is lower than the highest temperature (~1125 $^{\circ}\text{C}$) constrained by P–T pseudosection for the same granulite [43]. This discrepancy may be caused by the analytical effects, as Pape et al. [70] illustrated when they attempted to reintegrate the original Zr concentration in rutile due to the ZrO_2 exsolution. Since rutile and quartz differ in their chemistry, structure, and density, both phases show various absorption coefficients resulting in different characteristic X-ray efficiencies. Possible fluorescence effects due to rutile in quartz and the difference of the incident angle of electrons at the center and the spot periphery may bias analyses. Therefore, the high temperatures obtained by matrix

quartz using the 50 μm defocused beam reflect the absolute minimum temperatures for the peak metamorphic conditions. Since most analyses also yield temperatures above 900 $^{\circ}\text{C}$, the TitaniQ thermometer is reliable for recognizing UHT granulites even with exsolved rutile rods in quartz.

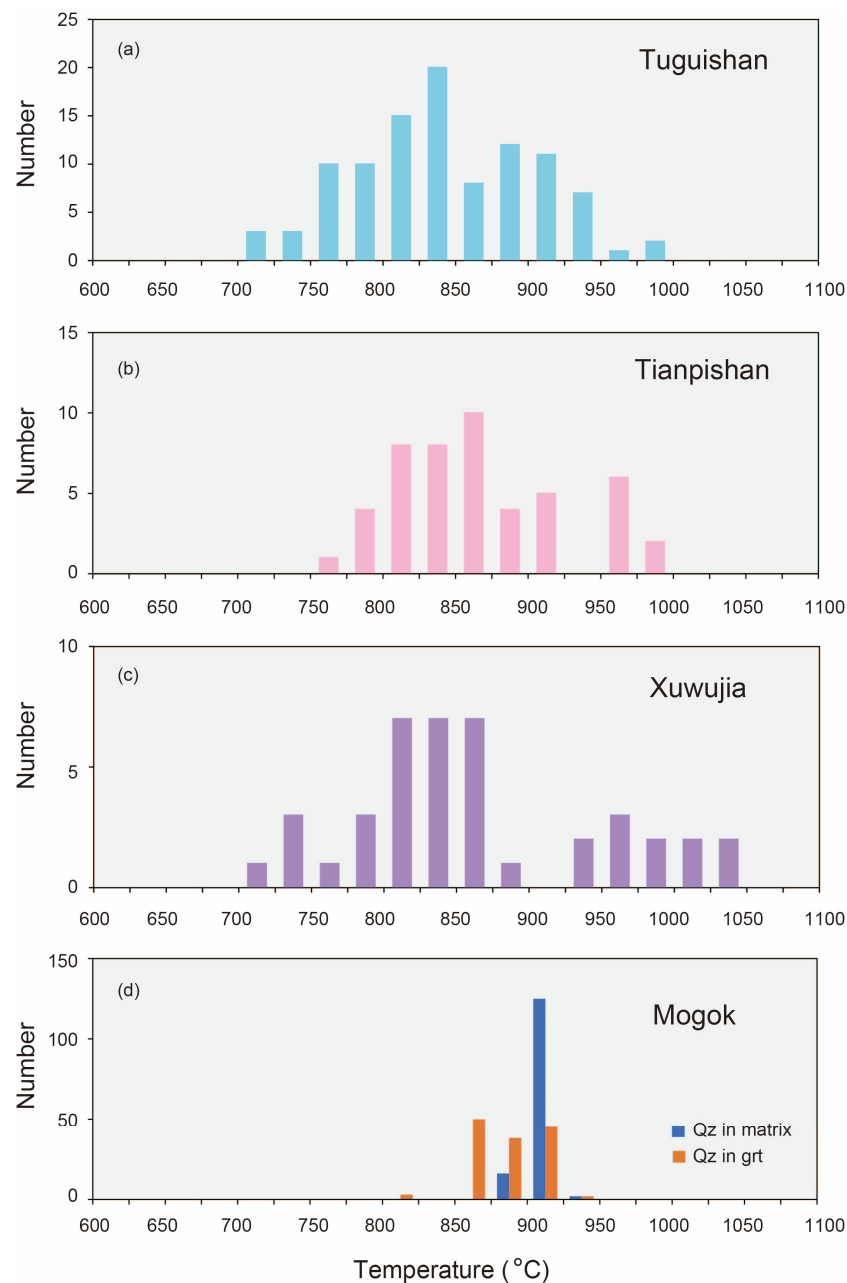


Figure 7. Comparison of the calculated temperatures of quartz from various areas. (a) Calculated temperatures of matrix quartz from Tuguishan (beam size: 50 μm). (b) Calculated temperatures of matrix quartz from Tianpishan (beam size: 50 μm). (c) Calculated temperatures of matrix quartz from Tianpishan (beam size: 50 μm). (d) Calculated temperatures of quartz from Mogok (beam size: 10 μm).

For the MMB granulites, the temperatures obtained by the matrix quartz (894–926 $^{\circ}\text{C}$, 909 ± 7 $^{\circ}\text{C}$) (Figure 6a) are in good agreement with those (890–940 $^{\circ}\text{C}$) constrained by the Zr-in-rutile thermometer and P–T pseudosections [54]. Thus, the TitaniQ thermometer can well constrain the peak temperatures of the MMB granulites.

Therefore, the TitaniQ thermometry combined with quartz textures can be used to estimate the peak or near-peak temperatures of UHT granulites, which would play an important role in identifying the regional distribution of UHT metamorphism.

6.2. Slow Cooling of UHT Granulites in KB

Generally, the UHT granulites in the Khondalite Belt have experienced complex clockwise P–T paths, including decompression heating, nearly isobaric cooling (IBC), and nearly isothermal decompression/decompression heating stages [38,39,41,71]. Geochronological studies indicate that the KB granulites experienced a long-lived HT–UHT metamorphism, followed by a slow post-peak cooling process [40,71–73]. Jiao et al. [74] proposed that the eastern KB experienced a long-lived post-peak cooling process (nearly 100 Ma) with a thermal peak at ~1.90 Ga and further cooling to ~1.80 Ga. Furthermore, thermometer calculation results also reflect the slow cooling process in the KB granulites. For example, the wide range of calculated temperatures (819–1037 °C) from two-feldspar thermometry points to a slow cooling process after the peak UHT metamorphism [39]. Low temperatures recorded by the Zr-in-rutile thermometer [39] also imply that the slow post-peak cooling process significantly affected the KB granulite rutile. However, the post-peak diffusion of Zr between rutile and other Zr-bearing minerals (such as zircon, baddeleyite, and ilmenite) is very complex [75], which hampers our understanding of the cooling behavior of UHT granulites.

Rutile rods in quartz and the low temperatures calculated by the TitaniQ thermometer could directly indicate the slow cooling of the KB UHT granulites. Under analytical conditions with 10 µm beam size, the Ti concentrations in quartz from the KB granulites vary significantly. Matrix quartz and quartz inclusions contain Ti of 57–241 ppm and 65–229 ppm, respectively, corresponding to the TitaniQ temperatures of 653–810 °C and 666–807 °C. Most estimated temperatures, concentrated in the range of 710–750 °C (Figure 5a), are consistent with the lower temperature range (700–750 °C) obtained by the Zr-in-rutile thermometer [39]. Consistency of the lowest Ti content (60–70 ppm) in quartz from the three areas (Tuguishan, Tianpishan, and Xuwujia) indicates a uniform cooling point, possibly representing the cooling temperature for the exsolution of rutile from pre-existing Ti-rich quartz. To sum up, the textural characteristics of rutile rods in quartz, the corresponding lower Ti concentrations and temperatures, combined with the long-lived post-peak cooling process (nearly 100 Ma) of the hosted granulites [40,71–74], indicate that such rutile exsolution highly likely occurred during the slow cooling stage. In this regard, analyzing Ti contents in pure quartz grains is insufficient to recover the peak temperatures of UHT granulites but could yield slow cooling temperatures after the peak.

6.3. Rapid Cooling of UHT Granulites in MMB

In contrast, the MMB granulite may experience a fast cooling process. Chen et al. [54] constrained the age of UHT metamorphism in the MMB as ~25 Ma, based on precise U–Pb dating results of metamorphic zircon rims. According to the $^{40}\text{Ar}/^{39}\text{Ar}$ ages of biotite, muscovite, and phlogopite from granites, marbles, gneisses, and mica schists in the MMB (mostly 22.7–15.8 Ma, [55–57]), the cooling stage took place at the Late Oligocene–Early Miocene. Therefore, the duration of post-peak cooling in the MMB is no more than 10 Ma, significantly shorter than that in the KB.

The fast cooling process can be seen in different quartz textures and Ti concentrations. Even using 10 µm beam size, the Ti concentrations in the MMB granulite quartz are higher than those from the KB. The Ti concentrations of quartz inclusions (107–267 ppm) and matrix quartz (207–260 ppm) record temperatures of 809–930 °C and 894–926 °C, respectively, which are higher than those of the KB granulite. The average temperature of matrix quartz is 909 ± 7 °C, corresponding to UHT metamorphic conditions. Note that the temperature range obtained by quartz inclusion is broader (809–930 °C) than those obtained by matrix quartz (894–926 °C) (Figure 7d). This feature could probably be attributed to the growth of quartz inclusions during prograde metamorphism. Considering the fast diffusion rate

in quartz [19], the small fluctuation of the Ti concentration (Figure 6b) and the absence of rutile rods indicate that the Ti diffusion is very weak in the MMB granulite, reflecting a fast cooling process. The rapid cooling could not provide enough time for rutile exsolution from the quartz lattice. In this regard, the Ti concentrations in quartz could reveal the prograde and peak metamorphic temperatures if UHT granulites underwent rapid cooling. The explicitly various texture characteristics, Ti concentration, and corresponding temperatures of quartz in granulites from these two UHT terranes indicate that the Ti behavior in quartz could well reflect various cooling rates caused by different uplift processes.

7. Conclusions

Trace elements of quartz grains in granulites from the KB, NCC, and the MMB Myanmar were analyzed using a precise EPMA analytical method. Even though the quartz samples share the same occurrence (as matrix minerals or as inclusions in garnet), their Ti concentrations obtained with a small defocused beam (10 μm) and the calculated temperatures vary greatly. The Ti concentrations of the KB granulite quartz are concentrated at 100–150 ppm due to the wide existence of exsolved rutile rods. The calculated temperatures of the TitaniQ thermometer are concentrated at 710–750 $^{\circ}\text{C}$, consistent with the post-peak stable temperatures recorded by the Zr-in-rutile thermometer. These results reflect a slow cooling process after UHT metamorphism. However, the Ti concentrations of the matrix quartz from the MMB granulites are generally as high as 207–260 ppm, corresponding to temperatures up to 894–926 $^{\circ}\text{C}$. These calculated values are consistent with the peak temperatures estimated by the P–T pseudosections and the Zr-in-rutile thermometer, indicating a UHT metamorphism followed by a rapid cooling process. Therefore, texture-based, precise analyses of the Ti concentrations in quartz can effectively reflect the cooling behavior of a metamorphic terrane. Our study also demonstrates that, using suitable beam sizes during EPMA analyses, the TitaniQ thermometer is a valuable tool for recovering UHT conditions.

Supplementary Materials: The following supporting information can be downloaded at: <https://www.mdpi.com/article/10.3390/cryst13071116/s1>, Figure S1: Detection limits (a,b) and standard deviations (c,d) for Al and Ti in the quartz reference standard as a function of accelerating voltage and beam current. Figure S2: Comparison of individual spectrometer detection limits (3σ) and standard deviation (3σ) of normal analyzing crystal (PET), large analyzing crystal (LPET), and the aggregate intensity counting method (2LPET) as a function of peak counting time (a,b) and beam current (c,d) as measured with the reference standard; Figure S3: Secondary fluorescence effects of Ti-in-quartz. (a) and (c) show the analysis spots beside the rutile grains. (b,d) exhibit the variation of Ti concentrations due to secondary fluorescence effects. Analysis was taken along the red lines. Table S1A: Analytical conditions for quartz analysis and detection limits for trace elements in the quartz reference standard.; Table S1B: Ti and Al concentrations (ppm) of the standard; Table S1C: Secondary fluorescence effects of Ti in quartz; Table S2: Ti concentrations (ppm) and calculated temperatures of the investigated samples from Tuguisan, Khondalite Belt, North China Craton; Table S3: Ti concentrations (ppm) and calculated temperatures of the investigated samples from Tianpisahn, Khondalite Belt, North China Craton; Table S4: Ti concentrations (ppm) and TitaniQ temperatures of the investigated samples from Xuwujia, Khondalite Belt, North China Craton; Table S5: Ti concentrations (ppm) and TitaniQ temperatures of the investigated samples from Htin Shu Taung, Mogok Metamorphic Belt, Myanmar; Table S6: Ti concentrations and the calculated temperatures of quartz profile in garnet from the MMB.

Author Contributions: Conceptualization, Y.C. and D.Z.; methodology, D.Z. and Q.M.; validation, Y.C. and D.Z.; formal analysis, D.Z.; investigation, D.Z. and B.S.; resources, S.J., S.C. and K.S.; data curation, D.Z.; writing—original draft preparation, D.Z.; writing—review and editing, Y.C.; visualization, D.Z.; supervision, Y.C.; project administration, Y.C.; funding acquisition, Y.C. All authors have read and agreed to the published version of the manuscript.

Funding: This work was supported by the National Science Foundation of China (42172064, 42202063) and the Experimental Technology Innovation Fund (11990890) of the Institute of Geology and Geophysics, Chinese Academy of Sciences.

Data Availability Statement: All data generated or analyzed during this study are included in this article and its supplementary information files.

Acknowledgments: We thank Andreas Audétat for providing the quartz reference standard and anonymous reviewers for their constructive comments.

Conflicts of Interest: The authors declare no conflict of interest.

References

1. Harley, S.L. Refining the P–T records of UHT crustal metamorphism. *J. Metamorph. Geol.* **2008**, *26*, 125–154. [[CrossRef](#)]
2. Jiao, S.; Guo, J. Paleoproterozoic UHT metamorphism with isobaric cooling (IBC) followed by decompression–heating in the Khondalite Belt (North China Craton): New evidence from two sapphirine formation processes. *J. Metamorph. Geol.* **2020**, *38*, 357–378. [[CrossRef](#)]
3. Kelsey, D.E.; Hand, M. On ultrahigh temperature crustal metamorphism: Phase equilibria, trace element thermometry, bulk composition, heat sources, timescales and tectonic settings. *Geosci. Front.* **2015**, *6*, 311–356. [[CrossRef](#)]
4. Harley, S.L. A matter of time: The importance of the duration of UHT metamorphism. *J. Mineral. Petrol. Sci.* **2016**, *111*, 50–72. [[CrossRef](#)]
5. Pattison, D.R.M.; Chacko, T.; Farquhar, J.; McFarlane, C.R.M. Temperatures of Granulite-facies Metamorphism: Constraints from Experimental Phase Equilibria and Thermobarometry Corrected for Retrograde Exchange. *J. Petrol.* **2003**, *44*, 867–900. [[CrossRef](#)]
6. Wu, J.; Zhang, H.; Zhai, M.; Zhang, H.; Wang, H.; Li, R.; Hu, B.; Zhang, H. Shared metamorphic histories of various Palaeoproterozoic granulites from Datong–Huai’an area, North China Craton (NCC): Constraints from zircon U–Pb ages and petrology. *Int. Geol. Rev.* **2019**, *61*, 694–719. [[CrossRef](#)]
7. Zack, T.V.; Von Eynatten, H.; Kronz, A. Rutile geochemistry and its potential use in quantitative provenance studies. *Sediment. Geol.* **2004**, *171*, 37–58. [[CrossRef](#)]
8. Watson, E.; Wark, D.; Thomas, J. Crystallization thermometers for zircon and rutile. *Contrib. Mineral. Petrol.* **2006**, *151*, 413–433. [[CrossRef](#)]
9. Ferry, J.; Watson, E. New thermodynamic models and revised calibrations for the Ti-in-zircon and Zr-in-rutile thermometers. *Contrib. Mineral. Petrol.* **2007**, *154*, 429–437. [[CrossRef](#)]
10. Tomkins, H.; Powell, R.; Ellis, D. The pressure dependence of the zirconium-in-rutile thermometer. *J. Metamorph. Geol.* **2007**, *25*, 703–713. [[CrossRef](#)]
11. Watson, E.B.; Harrison, T. Zircon thermometer reveals minimum melting conditions on earliest Earth. *Science* **2005**, *308*, 841–844. [[CrossRef](#)] [[PubMed](#)]
12. Wark, D.A.; Watson, E.B. TitaniQ: A titanium-in-quartz geothermometer. *Contrib. Mineral. Petrol.* **2006**, *152*, 743–754. [[CrossRef](#)]
13. Thomas, J.B.; Bruce Watson, E.; Spear, F.S.; Shemella, P.T.; Nayak, S.K.; Lanzirrotti, A. TitaniQ under pressure: The effect of pressure and temperature on the solubility of Ti in quartz. *Contrib. Mineral. Petrol.* **2010**, *160*, 743–759. [[CrossRef](#)]
14. Huang, R.; Audétat, A. The titanium-in-quartz (TitaniQ) thermobarometer: A critical examination and re-calibration. *Geochim. Cosmochim. Acta* **2012**, *84*, 75–89. [[CrossRef](#)]
15. Zhang, C.; Li, X.; Almeev, R.R.; Horn, I.; Behrens, H.; Holtz, F. Ti-in-quartz thermobarometry and TiO₂ solubility in rhyolitic melts: New experiments and parametrization. *Earth Planet. Sci. Lett.* **2020**, *538*, 116213. [[CrossRef](#)]
16. Altenberger, U.; Mejia Jimenez, D.; Günter, C.; Sierra Rodriguez, G.; Scheffler, F.; Oberhänsli, R. The Garzón Massif, Colombia—a new ultrahigh-temperature metamorphic complex in the Early Neoproterozoic of northern South America. *Mineral. Petrol.* **2012**, *105*, 171–185. [[CrossRef](#)]
17. Ewing, T.A.; Hermann, J.; Rubatto, D. The robustness of the Zr-in-rutile and Ti-in-zircon thermometers during high-temperature metamorphism (Ivrea-Verbano Zone, northern Italy). *Contrib. Mineral. Petrol.* **2012**, *165*, 757–779. [[CrossRef](#)]
18. Tual, L.; Möller, C.; Whitehouse, M. Tracking the prograde P–T path of Precambrian eclogite using Ti-in-quartz and Zr-in-rutile geothermobarometry. *Contrib. Mineral. Petrol.* **2018**, *173*, 56. [[CrossRef](#)]
19. Cherniak, D.; Watson, E.; Wark, D. Ti diffusion in quartz. *Chem. Geol.* **2007**, *236*, 65–74. [[CrossRef](#)]
20. Sato, K.; Santosh, M. Titanium in quartz as a record of ultrahigh-temperature metamorphism: The granulites of Karur, southern India. *Mineral. Mag.* **2007**, *71*, 143–154. [[CrossRef](#)]
21. Storm, L.; Spear, F. Application of the titanium-in-quartz thermometer to pelitic migmatites from the Adirondack Highlands, New York. *J. Metamorph. Geol.* **2009**, *27*, 479–494. [[CrossRef](#)]
22. Müller, A.; Wiedenbeck, M.; van den Kerkhof, A.M.; Kronz, A.; Simon, K. Trace elements in quartz—A combined electron microprobe, secondary ion mass spectrometry, laser-ablation ICP-MS, and cathodoluminescence study. *Eur. J. Mineral.* **2003**, *15*, 747–763. [[CrossRef](#)]
23. Jourdan, A.-L.V.; Mullis, J.; Ramseyer, K.; Spiers, C.J. Evidence of growth and sector zoning in hydrothermal quartz from Alpine veins. *Eur. J. Mineral.* **2009**, *21*, 219–231. [[CrossRef](#)]
24. Lehmann, K.; Berger, A.; Gotte, T.; Ramseyer, K.; Wiedenbeck, M. Growth related zonations in authigenic and hydrothermal quartz characterized by SIMS-, EPMA-, SEM-CL- and SEM-CC-imaging. *Mineral. Mag.* **2009**, *73*, 633–643. [[CrossRef](#)]
25. Behr, W.M.; Thomas, J.B.; Hervig, R.L. Calibrating Ti concentrations in quartz for SIMS determinations using NIST silicate glasses and application to the TitaniQ geothermobarometer. *Am. Mineral.* **2011**, *96*, 1100–1106. [[CrossRef](#)]

26. Donovan, J.J.; Lowers, H.A.; Rusk, B.G. Improved electron probe microanalysis of trace elements in quartz. *Am. Mineral.* **2011**, *96*, 274–282. [[CrossRef](#)]
27. Tanner, D.; Henley, R.W.; Mavrogenes, J.A.; Holden, P. Combining in situ isotopic, trace element and textural analyses of quartz from four magmatic-hydrothermal ore deposits. *Contrib. Mineral. Petrol.* **2013**, *166*, 1119–1142. [[CrossRef](#)]
28. Audétat, A.; Garbe-Schönberg, D.; Kronz, A.; Pettke, T.; Rusk, B.; Donovan, J.J.; Lowers, H.A. Characterisation of a Natural Quartz Crystal as a Reference Material for Microanalytical Determination of Ti, Al, Li, Fe, Mn, Ga and Ge. *Geostand. Geoanal. Res.* **2015**, *39*, 171–184. [[CrossRef](#)]
29. Cruz-Uribe, A.M.; Mertz-Kraus, R.; Zack, T.; Feineman, M.D.; Woods, G.; Jacob, D.E. A New LA-ICP-MS Method for Ti in Quartz: Implications and Application to High Pressure Rutile-Quartz Veins from the Czech Erzgebirge. *Geostand. Geoanal. Res.* **2016**, *41*, 29–40. [[CrossRef](#)]
30. Guillon, M.; Günther, D. Effect of particle size distribution on ICP-induced elemental fractionation in laser ablation-inductively coupled plasma-mass spectrometry. *J. Anal. At. Spectrom.* **2002**, *17*, 831–837. [[CrossRef](#)]
31. Sylvester, P.J. LA-(MC)-ICP-MS trends in 2006 and 2007 with particular emphasis on measurement uncertainties. *Geostand. Geoanal. Res.* **2008**, *32*, 469–488. [[CrossRef](#)]
32. Wu, S.T.; Xu, C.X.; Simon, K.; Xiao, Y.L.; Wang, Y.P. Study on Ablation Behaviors and Ablation Rates of a 193nm ArF Excimer Laser System for Selected Substrates in LA-ICP-MS analysis. *Rock Miner. Anal.* **2017**, *36*, 451–459.
33. Kendrick, J.; Indares, A. The Ti record of quartz in anatexitic aluminous granulites. *J. Petrol.* **2018**, *59*, 1493–1516. [[CrossRef](#)]
34. Zhao, G.; Sun, M.; Wilde, S.A.; Sanzhong, L. Late Archean to Paleoproterozoic evolution of the North China Craton: Key issues revisited. *Precambrian Res.* **2005**, *136*, 177–202. [[CrossRef](#)]
35. Santosh, M.; Tsunogae, T.; Li, J.; Liu, S. Discovery of sapphirine-bearing Mg–Al granulites in the North China Craton: Implications for Paleoproterozoic ultrahigh temperature metamorphism. *Gondwana Res.* **2007**, *11*, 263–285. [[CrossRef](#)]
36. Santosh, M.; Wan, Y.; Liu, D.; Chunyan, D.; Li, J. Anatomy of zircons from an ultrahot orogen: The amalgamation of the North China Craton within the supercontinent Columbia. *J. Geol.* **2009**, *117*, 429–443. [[CrossRef](#)]
37. Yin, C.; Zhao, G.; Sun, M.; Xia, X.; Wei, C.; Zhou, X.; Leung, W. LA-ICP-MS U–Pb zircon ages of the Qianlishan Complex: Constrains on the evolution of the Khondalite Belt in the Western Block of the North China Craton. *Precambrian Res.* **2009**, *174*, 78–94. [[CrossRef](#)]
38. Jiao, S.; Guo, J.; Mao, Q.; Zhao, R. Application of Zr-in-rutile thermometry: A case study from ultrahigh-temperature granulites of the Khondalite belt, North China Craton. *Contrib. Mineral. Petrol.* **2011**, *162*, 379–393. [[CrossRef](#)]
39. Jiao, S.; Guo, J. Application of the two-feldspar geothermometer to ultrahigh-temperature (UHT) rocks in the Khondalite belt, North China craton and its implications. *Am. Mineral.* **2011**, *96*, 250–260. [[CrossRef](#)]
40. Yang, Q.-Y.; Santosh, M.; Tsunogae, T. Ultrahigh-temperature metamorphism under isobaric heating: New evidence from the North China Craton. *J. Asian Earth Sci.* **2014**, *95*, 2–16. [[CrossRef](#)]
41. Li, X.; Wei, C. Ultrahigh-temperature metamorphism in the Tuguiwula area, Khondalite Belt, North China Craton. *J. Metamorph. Geol.* **2018**, *36*, 489–509. [[CrossRef](#)]
42. Li, X.; White, R.W.; Wei, C. Can we extract ultrahigh-temperature conditions from Fe-rich metapelites? An example from the Khondalite Belt, North China Craton. *Lithos* **2019**, *328*, 228–243. [[CrossRef](#)]
43. Wang, B.; Wei, C.-J.; Tian, W. Evolution of spinel-bearing ultrahigh-temperature granulite in the Jining complex, North China Craton: Constrained by phase equilibria and Monte Carlo methods. *Mineral. Petrol.* **2021**, *115*, 283–297. [[CrossRef](#)]
44. Guo, J.H.; Wang, S.S. ⁴⁰Ar–³⁹Ar age spectra of garnet porphyroblast: Implications for metamorphic age of high-pressure granulite in the North China Craton. *Acta Petrol. Sin.* **2001**, *17*, 436–442.
45. Barley, M.E.; Pickard, A.L.; Zaw, K.; Rak, P.; Doyle, M.G. Jurassic to Miocene magmatism and metamorphism in the Mogok metamorphic belt and the India-Eurasia collision in Myanmar. *Tectonics* **2003**, *22*, 1019–1030. [[CrossRef](#)]
46. Mitchell, A.H.G.; Htay, M.T.; Htun, K.M.; Win, M.N.; Oo, T.; Hlaing, T. Rock relationships in the Mogok metamorphic belt, Tatkon to Mandalay, central Myanmar. *J. Asian Earth Sci.* **2007**, *29*, 891–910. [[CrossRef](#)]
47. Searle, M.P.; Noble, S.R.; Cottle, J.M.; Waters, D.J.; Mitchell, A.H.G.; Hlaing, T.; Horstwood, M.S.A. Tectonic evolution of the Mogok metamorphic belt, Burma (Myanmar) constrained by U-Th-Pb dating of metamorphic and magmatic rocks. *Tectonics* **2007**, *26*, TC3014. [[CrossRef](#)]
48. Mitchell, A.; Chung, S.-L.; Oo, T.; Lin, T.-H.; Hung, C.-H. Zircon U–Pb ages in Myanmar: Magmatic–metamorphic events and the closure of a neo-Tethys ocean? *J. Asian Earth Sci.* **2012**, *56*, 1–23. [[CrossRef](#)]
49. Zhang, D.; Guo, S.; Chen, Y.; Li, Q.; Ling, X.; Liu, C.; Sein, K. ~25 Ma Ruby Mineralization in the Mogok Stone Tract, Myanmar: New Evidence from SIMS U–Pb Dating of Coexisting Titanite. *Minerals* **2021**, *11*, 536. [[CrossRef](#)]
50. Yonemura, K.; Osanai, Y.; Nakano, N.; Adachi, T.; Charusiri, P.; Zaw, T.N. EPMA U-Th-Pb monazite dating of metamorphic rocks from the Mogok Metamorphic Belt, central Myanmar. *J. Mineral. Petrol. Sci.* **2013**, *108*, 184–188. [[CrossRef](#)]
51. Thu, Y.K.; Win, M.M.; Enami, M.; Tsuboi, M. Ti-rich biotite in spinel and quartz-bearing paragneiss and related rocks from the Mogok metamorphic belt, central Myanmar. *J. Mineral. Petrol. Sci.* **2016**, *111*, 151020.
52. Win, M.M.; Enami, M.; Kato, T. Metamorphic conditions and CHIME monazite ages of Late Eocene to Late Oligocene high-temperature Mogok metamorphic rocks in central Myanmar. *J. Asian Earth Sci.* **2016**, *117*, 304–316. [[CrossRef](#)]
53. Thu, Y.K.; Enami, M.; Kato, T.; Tsuboi, M. Granulite facies paragneisses from the middle segment of the Mogok metamorphic belt, central Myanmar. *J. Mineral. Petrol. Sci.* **2017**, *112*, 1–19.

54. Chen, S.; Chen, Y.; Li, Y.; Su, B.; Zhang, Q.; Aung, M.M.; Sein, K. Cenozoic ultrahigh-temperature metamorphism in pelitic granulites from the Mogok metamorphic belt, Myanmar. *Sci. China: Earth Sci.* **2021**, *64*, 1873–1892. [[CrossRef](#)]
55. Bertrand, G.; Rangin, C.; Maluski, H.; Bellon, H. Diachronous cooling along the Mogok Metamorphic Belt (Shan scarp, Myanmar): The trace of the northward migration of the Indian syntaxis. *J. Asian Earth Sci.* **2001**, *19*, 649–659. [[CrossRef](#)]
56. Bertrand, G.; Rangin, C. Tectonics of the western margin of the Shan plateau (central Myanmar): Implication for the India–Indochina oblique convergence since the Oligocene. *J. Asian Earth Sci.* **2003**, *21*, 1139–1157. [[CrossRef](#)]
57. Garnier, V.; Maluski, H.; Giuliani, G.; Ohnenstetter, D.; Schwarz, D. Ar–Ar and U–Pb ages of marble-hosted ruby deposits from central and southeast Asia. *Can. J. Earth Sci.* **2006**, *43*, 509–532. [[CrossRef](#)]
58. Themelis, T. *Gems and Mines of Mogok*; A&T Pub.: Los Angeles, CA, USA, 2008.
59. Whitney, D.L.; Evans, B.W. Abbreviations for names of rock-forming minerals. *Am. Mineral.* **2010**, *95*, 185–187. [[CrossRef](#)]
60. Batanova, V.G.; Sobolev, A.V.; Kuzmin, D.V. Trace element analysis of olivine: High precision analytical method for JEOL JXA-8230 electron probe microanalyser. *Chem. Geol.* **2015**, *419*, 149–157. [[CrossRef](#)]
61. Ancy, M.; Bastenaire, F.; Tixier, R. Applications of statistical methods in microanalysis. In *Proc. Summer School St. Martin-d’Herres*; Maurice, F., Ed.; Les Editions de Physique: Orsay, France, 1978; pp. 319–343.
62. Thomas, J.B.; Watson, E.B.; Spear, F.S.; Wark, D. TitaniQ recrystallized: Experimental confirmation of the original Ti-in-quartz calibrations. *Contrib. Mineral. Petrol.* **2015**, *169*, 27. [[CrossRef](#)]
63. Osborne, Z.R.; Thomas, J.B.; Nachlas, W.O.; Baldwin, S.L.; Holycross, M.E.; Spear, F.S.; Watson, E.B. An experimentally calibrated thermobarometric solubility model for titanium in coesite (TitaniC). *Contrib. Mineral. Petrol.* **2019**, *174*, 34. [[CrossRef](#)]
64. Horton, F.; Hacker, B.; Kylander-Clark, A.; Holder, R.; Jöns, N. Focused radiogenic heating of middle crust caused ultrahigh temperatures in southern Madagascar. *Tectonics* **2016**, *35*, 293–314. [[CrossRef](#)]
65. Sanborn-Barrie, M.; Camacho, A.; Berman, R. High-pressure, ultrahigh-temperature 1.9 Ga metamorphism of the Kramanitua Complex, Snowbird Tectonic Zone, Rae Craton, Canada. *Contrib. Mineral. Petrol.* **2019**, *174*, 14. [[CrossRef](#)]
66. Ramírez-Salazar, A.; Almazán-López, M.D.M.; Colás, V.; Ortega-Gutiérrez, F. Multi-thermobarometry and microstructures reveal ultra-high temperature metamorphism in the Grenvillian Oaxacan Complex, Southern Mexico. *Int. Geol. Rev.* **2022**, *65*, 1331–1353. [[CrossRef](#)]
67. Zheng, Y.; Qi, Y.; Zhang, D.; Jiao, S.; Huang, G.; Guo, J. New Insight From the First Application of Ti-in-Quartz (TitaniQ) Thermometry Mapping in the Eastern Khondalite Belt, North China Craton. *Front. Earth Sci.* **2022**, *10*, 860057. [[CrossRef](#)]
68. Jiao, S.; Guo, J.; Harley, S.L.; Peng, P. Geochronology and trace element geochemistry of zircon, monazite and garnet from the garnetite and/or associated other high-grade rocks: Implications for Palaeoproterozoic tectonothermal evolution of the Khondalite Belt, North China Craton. *Precambrian Res.* **2013**, *237*, 78–100. [[CrossRef](#)]
69. Jiao, S.; Guo, J.; Harley, S.L.; Windley, B.F. New constraints from garnetite on the P–T path of the Khondalite Belt: Implications for the tectonic evolution of the North China Craton. *J. Petrol.* **2013**, *54*, 1725–1758. [[CrossRef](#)]
70. Pape, J.; Mezger, K.; Robyr, M. A systematic evaluation of the Zr-in-rutile thermometer in ultra-high temperature (UHT) rocks. *Contrib. Mineral. Petrol.* **2016**, *171*, 44. [[CrossRef](#)]
71. Li, X.; Wei, C. Phase equilibria modelling and zircon age dating of pelitic granulites in Zhaojiayao, from the Jining Group of the Khondalite Belt, North China Craton. *J. Metamorph. Geol.* **2016**, *34*, 595–615. [[CrossRef](#)]
72. Wan, Y.; Song, B.; Liu, D.; Wilde, S.A.; Wu, J.; Shi, Y.; Yin, X.; Zhou, H. SHRIMP U–Pb zircon geochronology of Palaeoproterozoic metasedimentary rocks in the North China Craton: Evidence for a major Late Palaeoproterozoic tectonothermal event. *Precambrian Res.* **2006**, *149*, 249–271. [[CrossRef](#)]
73. Cai, J.; Liu, F.L.; Liu, P.H.; Shi, J.R. Metamorphic P–T conditions and U–Pb dating of the sillimanite-cordierite-garnet paragneisses in Sanchakou, Jining area, Inner Mongolia. *Acta Petrol. Sin.* **2014**, *30*, 472–490.
74. Jiao, S.; Guo, J.; Evans, N.J.; McDonald, B.J.; Liu, P.; Ouyang, D.; Fitzsimons, I.C. The timing and duration of high-temperature to ultrahigh-temperature metamorphism constrained by zircon U–Pb–Hf and trace element signatures in the Khondalite Belt, North China Craton. *Contrib. Mineral. Petrol.* **2020**, *175*, 66. [[CrossRef](#)]
75. Chen, Y.; Chen, S.; Su, B.; Li, Y.B.; Gu, S. Trace element systematics of granulite facie rutile. *J. Earth Sci.* **2018**, *43*, 127–149.

Disclaimer/Publisher’s Note: The statements, opinions and data contained in all publications are solely those of the individual author(s) and contributor(s) and not of MDPI and/or the editor(s). MDPI and/or the editor(s) disclaim responsibility for any injury to people or property resulting from any ideas, methods, instructions or products referred to in the content.